Cyanido-Bridged Fe^{II}–M^{I} Dimetallic Hofmann-Like Spin-Crossover Coordination Polymers Based on 2,6-Naphthyridine

Lucía Piñeiro-López,[a] Francisco Javier Valverde-Muñoz,[a] Maksym Seredyuk,[a,b] Carlos Bartual-Murgui,[a] M. Carmen Muñoz,[c] and José Antonio Real*[a]

Dedicated to Professor Juan Faus Payá on the occasion of his retirement

Abstract: Two new 3D spin-crossover (SCO) Hofmann-type coordination polymers {Fe(2,6-naphthy)[$Ag(CN)_2$][$Ag_2(CN)_3$]} (**1**; 2,6-naphthy = 2,6-naphthyridine) and {Fe(2,6-naphthy)-[$Au(CN)_2$]$_2$}·0.5$PhNO_2$ (**2**) were synthesized and characterized. Both derivatives are made up of infinite stacks of {Fe[$Ag(CN)_2$]$_2$-[$Ag_2(CN)_3$]}$_n$ and {Fe[$Au(CN)_2$]$_2$}$_n$ layered grids connected by pillars of 2,6-naphthy ligands coordinated to the axial positions of the Fe^{II} centers of alternate layers. The in situ generated [$Ag_2(CN)_3$]$^-$ linkers define wide rectangular windows that favor the interpenetration of three identical 3D networks, strong argentophilic interactions between them, and the generation of a densely packed structure without accessible void spaces. In contrast, the smaller rhombus-shaped window in **2** affords a structure made up of doubly interpenetrated 3D networks with strong aurophilic interactions between them and accessible voids partially occupied by nitrobenzene molecules. Compound **1** displays a relatively abrupt two-step SCO in the temperature interval 150–215 K, whereas **2** features an incomplete one-step SCO behavior ($T_{1/2}$ = 166 K) that extends over 150 K.

Introduction

Iron(II) spin-crossover (SCO) complexes are a well-known class of switchable molecular materials. The switch between the high-spin (HS) and low-spin (LS) states occurs in a reversible, controllable, and detectable manner triggered by external stimuli (i.e., temperature, pressure, light, or guest molecules) and involves changes to the molecular structure, magnetism, color, and electrical polarizability.[1] The different size of the Fe^{II} ion in both electronic states is at the origin of cooperative elastic interactions between the SCO centers in the crystal.[2] If these interactions are strong enough, the SCO material exhibits bistability, an appealing property with potential applications in the construction of molecular devices for information storage, signal processing, and sensing.[3] In this respect, the possible processing of SCO materials at micro- and nanometric scales or even at the single-molecule level has aroused much interest in recent years in the areas of molecular nanoelectronics and spintronics.[4]

The design and synthesis of new SCO materials is a necessary step to discover interesting SCO behavior and possible applications. The impressive cooperative properties displayed by the first 1D and 2D 1,2,4-triazole-based Fe^{II} SCO coordination polymers suggested that the cooperativity could be enhanced through the replacement of the intermolecular interactions between the SCO centers with more reliable coordination bonds afforded by suitable bridging ligands.[5,3d] Consequently, the polymeric approach has been explored systematically from the 1990s, and several relevant 2D and 3D SCO coordination polymers (SCO-CPs) and porous metal–organic frameworks (SCO-MOFs) have been obtained.[6]

One of the most prolific series of SCO-CPs/SCO-MOFs are constituted by cyanido-bridged Fe–$M^{I,II}$ dimetallic 2D and 3D Hofmann-like compounds. In particular, the use of dicyanometallate linkers such as [$M^{I}(CN)_2$]$^-$ (M^{I} = Ag^{I} and Au^{I}) has expanded since the first 3D complexes {Fe(L)$_x$[$Ag^{I}(CN)_2$]$_2$} were reported in 2002.[7] In particular, the complex {Fe(pz)[$Ag^{I}(CN)_2$]$_2$} (pz = pyrazine) is prototypal of a series of SCO complexes generically formulated as {Fe(L)[$M^{I}(CN)_2$]$_2$} (M^{I} = Ag and Au), in which L is a bis-monodentate bridging pyridine-like ligand. The linear [$M^{I}(CN)_2$]$^-$ anions occupy the equatorial coordination positions of the Fe^{II} ions and define an infinite stack of 2D [Fe{$M^{I}(CN)_2$}$_2$]$_\infty$ layers connected by pillars of the bridging ligand L, which occupies the axial positions of the Fe^{II} ions. The layers are organized in such a way that the ligands L thread the meshes of adjacent sheets to generate two identical interpenetrated 3D networks with the α-Po topology (Scheme 1). Although {Fe(pz)[$Ag^{I}(CN)_2$]$_2$} displays a gradual and incomplete transition with hysteresis above 300 K,[8a] the homologous Au^{I} derivative displays a cooperative SCO between 367 and 349 K.[8b] Even more cooperative SCO between 261 and 223 K has been observed for the corre-

[a] *Institut de Ciència Molecular (ICMol), Departament de Química Inorgànica, Universitat de València, C/ Catedrático José Beltrán Martínez, 2, 46980 Paterna (Valencia), Spain E-mail: jose.a.real@uv.es www.uv.es/smolmat*

[b] *Department of Chemistry, Taras Shevchenko National University of Kyiv, Volodymyrska St. 64/13, Kyiv 01601, Ukraine*

[c] *Departament de Física Aplicada, Universitat Politècnica de València, Camino de Vera s/n, 46022 Valencia, Spain*

sponding Au^{I} derivative with 2-fluoropyrazine (Fpz).[9] Notably, for longer bridging ligands such as 3,6-bis(4-pyridyl)-1,2,4,5-tetrazine (bipytz),[10] 1,4-bis(pyridin-4-ylmethyl)piperazine (bpmp),[11] 2,5-bis(pyrid-4-yl)pyridine (bpp),[12] or 1,4-di(pyridin-4-yl)benzene (dpb,[13] Scheme 1) and M^{I} = Au, interesting inclusion chemistry and cooperative SCO behavior have been described despite the interpenetration of the networks. In summary, the use of different organic ligands and cyanometallate anions has resulted in a Hofmann-type family, which exhibits customized SCO behavior coupled with other interesting properties.[6]

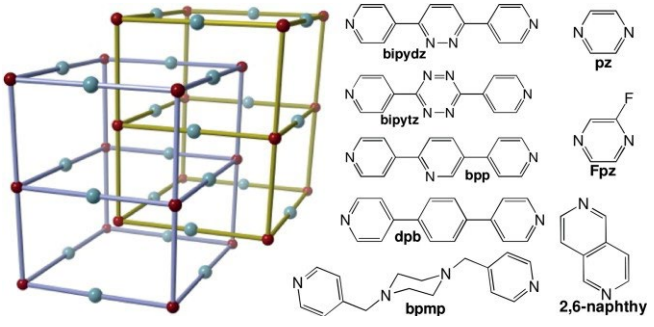

Scheme 1. Schematic view of two interpenetrated 3D networks with the α-Po topology and representations of the mentioned ligands.

Continuing this work, herein, we report the synthesis, crystal structures, and physical properties of two new Fe^{II} SCO systems based on the bis-monodentate organic ligand 2,6-naphthyridine (2,6-naphthy), namely, {Fe(2,6-naphthy)[$Ag(CN)_2$]-[$Ag_2(CN)_3$]} (**1**) and {Fe(2,6-naphthy)[$Au(CN)_2]_2$} 0.5$PhNO_2$ (**2**).

Results

Synthesis

The 2,6-naphthy ligand was synthetized by a modified synthetic route (Supporting Information, Section 1.8.1). Single crystals of **1** and **2** were synthesized by slow liquid–liquid diffusion techniques in a modified (common) H-vessel tube. Red and yellow rodlike single crystals of **1** and **2**, respectively, formed in relatively high yields (ca. 50 %) after four weeks. In particular, the relatively rare $[Ag_2(CN)_3]^-$ species occurs in **1**; $[Ag_2(CN)_3]^-$ has been identified previously in the crystals of some related SCO-CPs[14] but, to the best of our knowledge, has never been observed in solution or isolated in crystals as discrete anions of single salts. The incorporation of either $[Ag(CN)_2]^-$ anions or a mixture of $[Ag(CN)_2]^-$ and $[Ag_2(CN)_3]^-$ anions into the final polymer is most likely the result of competition between the two moieties and their associated equilibria [Equations (1) and (2)]. This competition seems to be influenced by the solvent, reagent concentrations, and overall stability and solubility of the final product. For **1**, a low concentration of $[Ag^{I}(CN)_2]^-$ anions and extended reaction times (liquid–liquid diffusion method) seem to favor the dissociation of $[Ag^{I}(CN)_2]^-$ anions to give $[Ag^{I}_2(CN)_3]^-$ anions. However, under the chosen experimental conditions, the synthesis of **1** is perfectly reproducible.

$$[Ag^{I}(CN)_2]^- \leftrightarrow CN^- + Ag^{I}CN \quad (1)$$

$$Ag^{I}CN + [Ag^{I}(CN)_2]^- \leftrightarrow [Ag^{I}_2(CN)_3]^- \quad (2)$$

The presence and quantification of the nitrobenzene molecules in **2** were confirmed by single-crystal X-ray diffraction studies and thermogravimetric analysis (Figure S1).

Magnetic Properties

The plot of $x_M T$ versus T for **1** (x_M is the molar magnetic susceptibility, and T is the temperature) is displayed in Figure 1 (top). At 250 K, the $x_M T$ value of ca. 3.75 cm^3 K mol^{-1} is consistent with all Fe^{II} centers in the HS state, and $x_M T$ remains constant down to 198 K. Then, upon cooling, the decrease of $x_M T$ in two marked steep steps to ca. 0.12 cm^3 K mol^{-1} at 170 K indicates the occurrence of a complete HS→LS spin transition. The heating mode does not match the cooling mode, and a narrow asymmetric hysteresis loop (ca. 6 K on average) is observed. The equilibrium temperatures $T_{1/2}$, at which the molar fraction of the HS and LS species is 50 %, are $T^{\downarrow}_{1/2}$ = 189 K and $T^{\uparrow}_{1/2}$ = 195 K for the cooling and heating modes, respectively, at a temperature scan rate of 1 K min^{-1}.

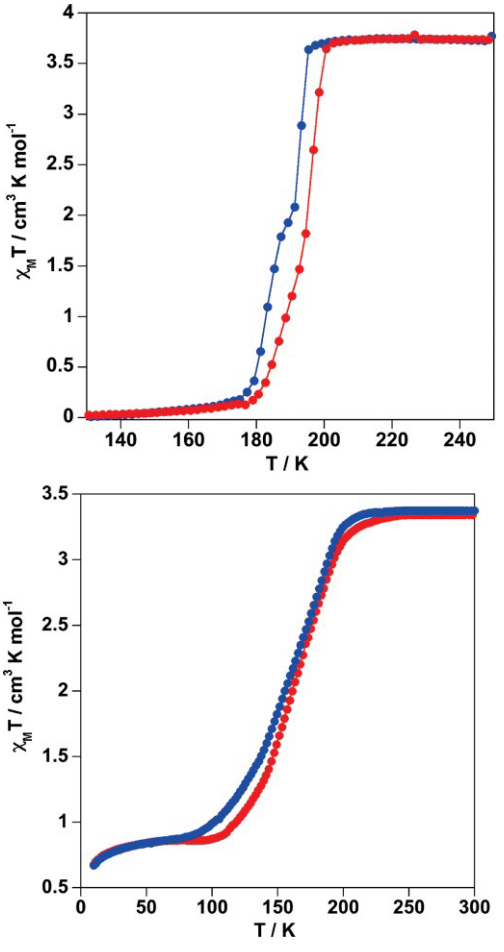

Figure 1. Magnetic behaviors displayed by **1** (top) and **2** (bottom). The cooling and heating modes are shown in blue and red, respectively.

The temperature dependence of the $x_M T$ product for **2** at 1 K min^{-1} is displayed in Figure 1 (bottom). The $x_M T$ value is ca.

3.35 cm^3 K mol^{-1} at 300 K, and it remains constant down to 220 K. Then, x_MT value decreases gradually upon cooling to attain a value of 0.84 cm^3 K mol^{-1} at 50 K. Below this temperature, x_MT decreases slightly, most probably because of the zero-field splitting of the Fe^{II} centers that remain HS at low temperature. Indeed, 75 % of the Fe^{II} centers in **2** undergo a spin transition from the HS state to the LS state. In the heating mode, the x_MT values do not match those observed for the cooling mode, and an unsymmetrical hysteresis is observed in the low temperature range (ca. 100–150 K), but the hysteresis practically disappears at higher temperatures. This behavior could be attributed to steric effects induced by the nitrobenzene molecules hosted in the pores and small kinetic effects that do not allow the system to reach the thermodynamic equilibrium even at temperature scan rates of 1 K min^{-1}. For a hypothetical complete SCO for **2**, the equilibrium temperatures are $T^{\downarrow}_{1/2}$ = 145 K and $T^{\uparrow}_{1/2}$ = 152 K.

Calorimetric Studies

Differential scanning calorimetry (DSC) measurements were performed for **1**. The temperature scan rate in the cooling and heating modes was 10 K min^{-1}. The anomalous variations of the molar specific heat caused by the SCO for the cooling and heating modes are displayed in Figure 2 in the form of ΔC_p versus T plots. The ΔC_p versus T plot shows the presence of two well-separated peaks in the cooling mode, whereas the peaks overlap in the heating mode and reflect the changes in the slope observed in the x_MT versus T curve of **1**. Moreover, each peak is reminiscent of those observed in the $\partial(x_MT)/\partial T$ versus T plot (Figure S2). The obtained critical temperatures ($T^{\downarrow}_{1/2}$ = 188 K and $T^{\uparrow}_{1/2}$ = 201 K) reproduce those obtained from the magnetic data. The average enthalpy and entropy variations associated with the cooling and heating modes (ΔH = 14.0 kJ mol^{-1} and ΔS = 71.6 J K^{-1} mol^{-1}) are consistent with the values typically displayed by Hofmann-like Fe^{II} clathrates featuring strong cooperative SCO behavior.[6] DSC measurements could not be performed for **2** because the temperature window of the spin transition for this compound extends beyond the limits of our calorimeter.

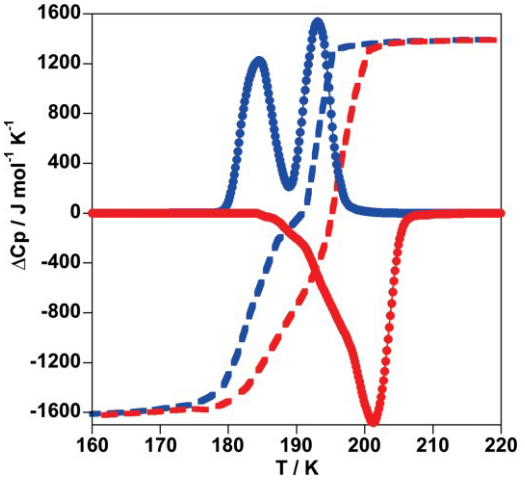

Figure 2. Calorimetric properties of **1**. The magnetic behavior of **1** is included as a reference (dashed lines). The blue and red lines correspond to the cooling and heating modes, respectively.

Structure

Single-crystal X-ray diffraction studies were performed for **1** at 150 and 250 K and for **2** at 250 K. A selection of significant bond lengths [Å], angles [°] and relevant crystallographic data are collected in Tables 1, 2, and 3, respectively.

Table 1. Selected bond lengths [Å] for **1** and **2**.

	1 (250 K)	**1** (150 K)	**2** (250 K)
Fe–N(1)	2.264(14)	2.006(14)	2.242(13)
Fe–N(2)	2.228(13)	2.01(2)	2.237(13)
Fe–N(3)	2.147(14)	1.91(2)	2.134(14)
Fe–N(4)	2.148(14)	1.931(14)	2.14(2)
Fe–N(5)	2.14(2)	1.95(2)	2.127(12)
Fe–N(6)	2.16(2)	1.95(2)	2.158(14)
Ag(1)–C(9)	2.048(14)	2.04(2)	–
Ag(1)–C(10)	2.06(2)	2.03(2)	–
Ag(2)–C(12)	2.04(2)	2.05(2)	–
Ag(2)–C(13)	2.06(2)	2.08(2)	–
Ag(3)–C(11)	2.02(2)	2.03(2)	–
Ag(2)–N(7)	2.08(2)	2.09(2)	–
Ag(1)–Ag(2)	3.121(2)	3.024(3)	–
Ag(1)–Ag(3)	3.281(2)	3.147(3)	–
Ag(2)–Ag(3)	3.236(2)	3.114(2)	–
Au(1)–C(9)	–	–	2.02(2)
Au(1)–C(10)	–	–	1.97(2)
Au(2)–C(11)	–	–	1.96(2)
Au(2)–C(12)	–	–	1.98(2)
Au(1)–Au(2)	–	–	3.1606(12)
$[FeN_6]^{ave}$	2.181	1.960	2.173

Table 2. Selected angles [°] for **1** and **2**.

	1 (250 K)	**1** (150 K)	**2** (250 K)
N(1)–Fe–N(2)	178.3(5)	178.4(6)	178.3(5)
N(1)–Fe–N(3)	87.5(5)	88.1(6)	89.7(5)
N(1)–Fe–N(4)	90.8(6)	90.4(6)	90.6(5)
N(1)–Fe–N(5)	87.7(6)	89.0(6)	89.8(5)
N(1)–Fe–N(6)	91.8(5)	91.1(6)	89.3(5)
N(2)–Fe–N(3)	91.4(5)	91.2(6)	88.9(6)
N(2)–Fe–N(4)	90.3(6)	90.3(6)	90.8(5)
N(2)–Fe–N(5)	91.1(6)	89.7(6)	89.2(5)
N(2)–Fe–N(6)	89.6(5)	90.4(6)	91.7(5)
N(3)–Fe–N(4)	176.1(8)	178.1(6)	179.5(5)
N(3)–Fe–N(5)	94.5(7)	94.9(7)	90.7(5)
N(3)–Fe–N(6)	92.3(7)	93.2(7)	89.6(5)
N(4)–Fe–N(5)	88.9(7)	86.3(7)	88.9(6)
N(4)–Fe–N(6)	84.2(6)	85.6(7)	90.8(6)
N(5)–Fe–N(6)	173.1(5)	171.9(6)	179.1(5)
C(9)–Ag(1)–C(10)	176.4(9)	175.7(9)	–
C(12)–Ag(2)–C(13)	171.6(7)	170.0(7)	–
C(11)–Ag(3)–N(7)	177.2(8)	175.6(8)	–
N(3)–C(9)–Ag(1)	178(2)	178(2)	–
N(4)–C(10)–Ag(1)	174(2)	176(2)	–
N(6)–C(12)–Ag(2)	175(2)	169(2)	–
N(7)–C(13)–Ag(2)	173(2)	173(2)	–
N(5)–C(11)–Ag(3)	171(2)	164(2)	–
C(9)–Au(1)–C(10)	–	–	176.9(8)
C(11)–Au(2)–C(12)	–	–	177.9(7)
N(3)–C(9)–Au(1)	–	–	179(2)
N(4)–C(10)–Au(1)	–	–	176(2)
N(5)–C(11)–Au(2)	–	–	178(2)
N(6)–C(12)–Au(2)	–	–	178(2)
Σ	24.3	22.8	9.2

Compound **1** displays the monoclinic non-centrosymmetric *Pc* space group irrespective of temperature. The structural motifs in this material are essentially the same at both temperatures; thus, the crystal structure at 150 K is analyzed representatively and compared with that found at 250 K. All of the Fe atoms are crystallographically equivalent, whereas three independent Ag atoms can be seen in the asymmetric unit at both temperatures. Each Fe atom defines an axially elongated [FeN_6] octahedron with its axial positions occupied by two nitrogen atoms of two equivalent 2,6-naphthy ligands. The equatorial positions are occupied by four nitrogen atoms of two equivalent pairs of $[Ag(CN)_2]^-$ and $[Ag_2(CN)_3]^-$ anions (Figure 3). The average bond lengths <Fe–N> are 1.96 and 2.18 Å at 150 and 250 K, respectively. This corresponds to a variation of ca. 0.22 Å between the LS and HS states, which is consistent with a complete spin transition. The sum of the deviations from the ideal octahedron of the 12 "*cis*" N–Fe–N angles ($\Sigma = \sum_{i=1}^{12} |\theta_i - 90|$) shows that the coordination center is weakly distorted in the HS state with $\Sigma = 24.3°$, and this value decreases slightly in the LS state to 22.8°.

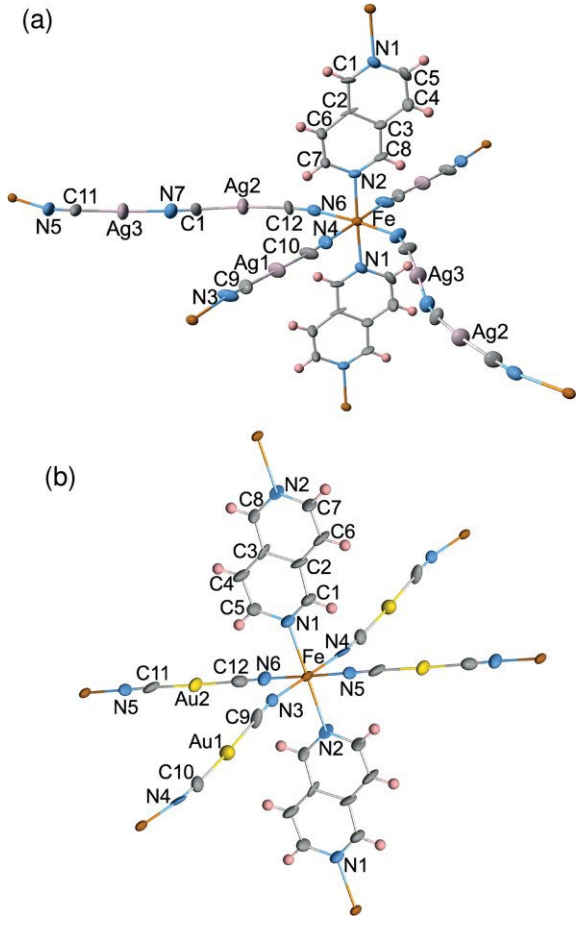

Figure 3. ORTEP representations of the representative molecular fragments for (a) **1** and (b) **2** (thermal ellipsoids are shown at 40 % probability).

The equatorial $[Ag(CN)_2]^-$ and $[Ag_2(CN)_3]^-$ units act as bis-monodentate bridges to connect equivalent [FeN_6] units and, thereby, define an infinite set of parallel flat $\{Fe[Ag(CN)_2][Ag_2(CN)_3]\}_\infty$ layers, which stack along the [100] direction. The grids are defined by rectangular $\{Fe[Ag^I(CN)_2][Ag^I_2(CN)_3]\}_\infty$ motifs (Figure 4a and b). The almost linear $[Ag^I(CN)_2]^-$ anions connect the Fe^{II} centers along the [010] direction with Fe···Fe distances of 10.255(6) and 10.624(3) Å at 150 and 250 K, respectively. In contrast, the markedly bent conformation of the $[Ag_2(CN)_3]^-$ anions leads to corrugated –{Fe–$[Ag_2(CN)_3]$–Fe}– chains along [001] with Fe···Fe distances of 15.0(2) and 15.25(8) Å at 150 and 250 K, respectively (Figure 4a). In turn, the 2,6-naphthy ligands, which are axially coordinated to the iron atoms [the Fe···Fe distances are 8.991(7) and 9.376(4) Å at 150 and 250 K, respectively; Figure 4c], act as pillars to connect the alternate layers along [100] and, thus, define an open 3D framework with a distorted α-Po topology. In addition, these links "thread" the meshes of two adjacent networks to enable the triple interpenetration of three identical 3D networks (Figure 4d). Moreover, coupled with the SCO phenomenon, strong argentophilic interactions occur between these 3D networks (Figure S3).

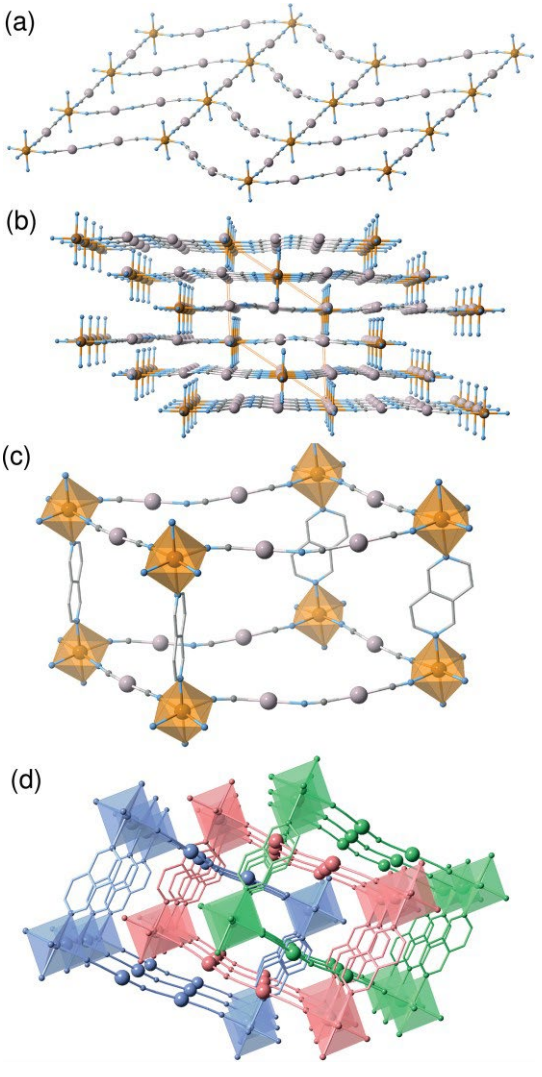

Figure 4. Compound **1**: (a) Fragment of a flat $\{Fe[Ag^I(CN)_2][Ag^I_2(CN)_3]\}_\infty$ layer. (b) Stacking of 6 consecutive layers. (c) Two layers connected by pillars of 2,6-naphthy ligands. (d) Three interpenetrated α-Po-type frameworks. Yellow = Au, blue = N, grey = C, orange = Fe.

The structural analysis of **2** at 250 K shows that this compound crystallizes in the triclinic $P\bar{1}$ space group and contains equivalent Fe^{II} centers. The iron atom defines an elongated $[FeN_6]$ octahedron that is coordinated equatorially by two pairs of crystallographically independent $[Au(CN)_2]^-$ groups, whereas the axial positions are occupied by two equivalent 2,6-naphthy ligands (Figure 5). The average <Fe–N> bond length of 2.17(2) Å is consistent with HS Fe^{II} centers, in agreement with the magnetic data at the same temperature. The angular distortion represented by the parameter $\Sigma = 9.2°$ indicates that the octahedron is more regular than that of **1**.

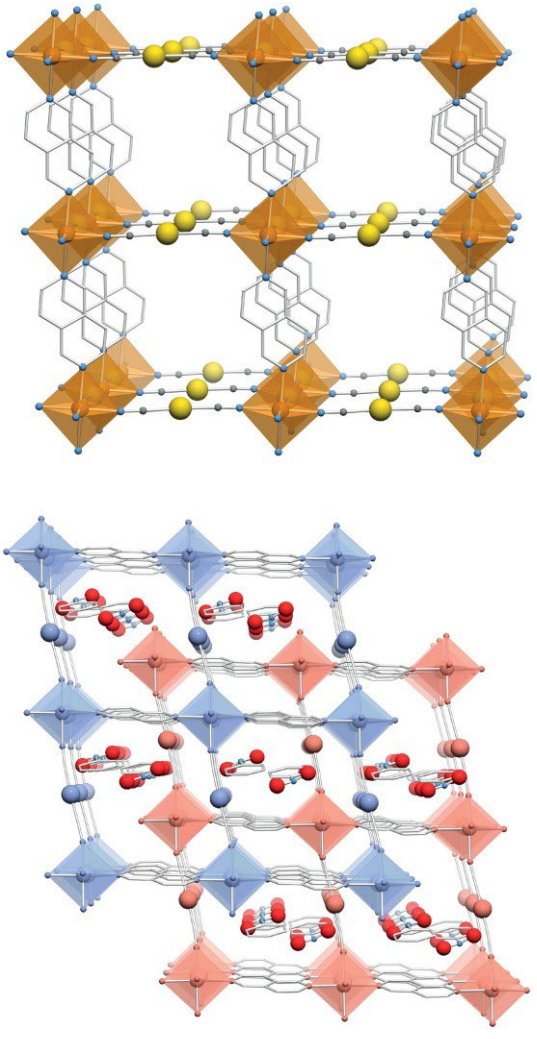

Figure 5. Compound **2**: Top: fragment of the 3D framework with the α-Po-type network. Bottom: interpenetration of two identical networks showing intercalated nitrobenzene molecules. Yellow = Au, blue = N, grey = C, orange = Fe.

The equatorial $[Au(CN)_2]^-$ groups act as bridges that link the Fe centers and, thereby, define a 2D $\{Fe[Au(CN)_2]_2\}_\infty$ grid-layered structure parallel to the *bc* plane. The grid structure is made up of edge-shared $\{Fe_4[Au(CN)_2]_4\}$ rhombuses defined by iron atoms and $[Au(CN)_2]^-$ linkers [the Fe···Fe distances are 10.497(3) and 10.475(3) Å]. The almost flat layers stack along [100] and are connected by pillars of 2,6-naphthy ligands through the axial positions of the Fe centers to form chains that propagate along the *a* axis, and the Fe···Fe distance mediated by 2,6-naphthy is 9.455(3) Å (Figure 5). The resulting 3D α-Po-type framework exhibits a much more regular geometry than that described for **1**.

The large void space generated by the framework allows the interpenetration of two identical 3D networks. The iron atoms of one $\{Fe[Au(CN)_2]_2\}_\infty$ layer are situated below or above but displaced from the center of the $\{Fe_4[Au(CN)_2]_4\}$ square grids of the other layer (Figure 5, bottom). Interestingly, strong aurophilic interactions [the Au···Au distance is ca. 3.16(1) Å] are observed between the two perpendicular edges of the $\{Fe_4[Au(CN)_2]_4\}$ square grids of the two closest layers (Figure S4). Despite the interpenetration, this 3D expanded Hofmann-like topology displays a channel along the *c* axis in which disordered nitrobenzene molecules are located (Figure 5, bottom). Short C···C contacts (smaller than the sum of the van der Waals radii of ca. 3.7 Å) evidence the occurrence of host–guest π–π intermolecular interactions (Figure S5 and Table S1). After the removal of the guest molecules with the SQUEEZE routine, the void space was calculated to be 348.6 $Å^3$ per unit cell, which corresponds to 34.3 % of the total volume. The analysis of the crystal structure of **2** near the LS state was not possible, as the single crystals cracked at low temperature.

Discussion

Fe^{II} Hofmann-like 3D SCO-CPs derived from $[M^I(CN)_2]^-$ (M^I = Ag, Au) building blocks have received less attention than those constituted of $[M^{II}(CN)_4]^{2-}$ (M^{II} = Ni, Pd, Pt) building blocks. $[M^I(CN)_2]^-$ (M^I = Ag, Au) linkers generate more-open frameworks than $[M^{II}(CN)_4]^{2-}$ linkers, a fact that favors interpenetration and reduces the effective size of the pores. In addition, the $[Ag(CN)_2]^-$ linker is not coordinatively inert and can expand the coordination number from two (linear) to three (T-shaped or trigonal)[15] and even four (tetrahedral)[16] to afford more complex 3D networks. Furthermore, in rare cases, the $[Ag(CN)_2]^-$ linkers acts as chemically unstable anions and afford in situ generated $[Ag_2(CN)_3]^-$ species. The first observation of this building block in a SCO-CP was described for $\{Fe(pmd)[Ag(CN)_2][Ag_2(CN)_3]\}$ (pmd = pyrimidine).[17] The replacement of the linear organic linker 2,6-naphthy with an angular linker such as pmd with a distinct orientation of the N donor atoms produces a very different and complicated 3D framework compared with that of **1**.

In both cases, the organic ligand acts as a bis-monodentate bridge to generate infinite –[Fe–2,6-naphthy–Fe]–$_\infty$ or –[Fe–pmd–Fe]–$_\infty$ parallel chains (Scheme 2). However, the pmd ligand imposes a 62° dihedral angle between the equatorial coordination planes of the $[FeN_6]$ octahedra occupied by the $[Ag(CN)_2]^-$ and $[Ag_2(CN)_3]^-$ units (Scheme 2); therefore, it is impossible to form a simple stack of $\{Fe[Ag(CN)_2][Ag_2(CN)_3]\}$ layers connected by pillars, as described for **1**, and generate an intricate self-interpenetrated 3D CP. Interestingly, the use of the slightly shorter pz ligand instead of 2,6-naphthy does not favor the formation of $[Ag_2(CN)_3]^-$ to afford $\{Fe(pz)[Ag(CN)_2]_2\}$, which exhibits the prototypal double-interpenetrated α-Po network shown in Scheme 1. In contrast, $[Ag_2(CN)_3]^-$ anions are gener-

ated through the self-assembly of Cd^{II} cations, pz ligands, and $[Ag(CN)_2]^-$ anions to afford $\{Cd^{II}(pz)[Ag(CN)_2][Ag_2(CN)_3]\}$,[18] which shares the triply interpenetrated expanded version of $\{Fe(pz)[Ag(CN)_2]_2\}$ with **1**.[7]

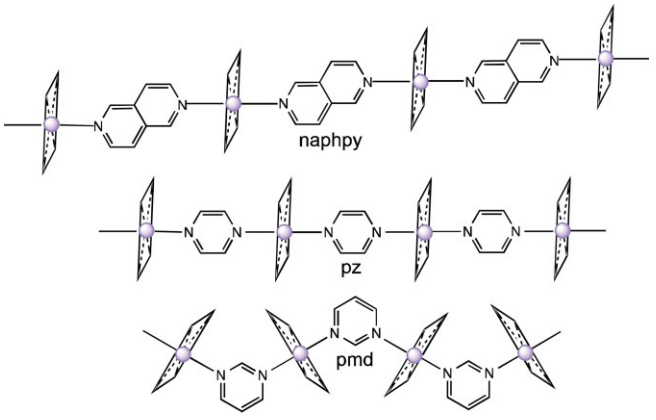

Scheme 2. Propagation of the $\{Fe(L)\}_n$ chains defined by the organic bis-monodentate bridging organic ligand L (see text).

There are two additional examples of 3D SCO-CPs with $[Ag^I_2(CN)_3]^-$ building blocks. One is $\{Fe(3,5\text{-}CH_3py)[Ag_2(CN)_3][Ag(CN)_2]\}$ (3,5-CH_3py = 3,5-dimethylpyridine), in which the monodentate nature of the axial organic ligand transforms the Fe^{II} centers into planar nodes with a coordination number of four to afford an expanded version of the prototypal structure of $CdSO_4$.[14b] Given the open nature of this framework, the crystal packing of the 3,5-CH_3py derivative consists of three identical interpenetrated subnets. The other example is $\{Fe(dpb)[Ag(CN)_2][Ag_2(CN)_3]\}\cdot n$Solvent [dpb is the long bridging ligand 1,4-di(pyridin-4-yl)benzene, Scheme 1].[14c] This compound displays a very complicated porous 3D framework that can be deconstructed into two identical interpenetrated networks with the $CdSO_4$ topology in which the "pseudo-square-planar" Fe^{II} nodes are defined by the dpb and $[Ag(CN)_2]^-$ bridges, and the $[Ag_2(CN)_3]^-$ groups can be seen as connectors between the two $CdSO_4$ subnets.

A common characteristic of the pmd, 3,5-CH_3py, and 2,6-naphthy SCO-CPs is the occurrence of more or less marked incipient two-step SCO. Moreover, **1** displays a moderate cooperativity characterized by an unsymmetrical hysteresis loop ca. 6 K wide. In contrast, the dpb derivative with the longer organic bridging ligand favors the presence of voids occupied by solvent molecules, which influence the completeness of the transition. In particular, for $\{Fe(dpb)[Ag(CN)_2][Ag_2(CN)_3]\}\cdot 2DMF\cdot CH_3CN$ (DMF = *N*,*N*-dimethylformamide), the two-step SCO extends over a wide temperature range (200–75 K) and exhibits a hysteresis loop ca. 10 K wide. Apparently, the presence of $[Ag(CN)_2]^-$ and $[Ag_2(CN)_3]^-$ anions confers some degree of flexibility to the framework and enables the accommodation of the $[FeN_6]$ structural changes during the SCO, a fact that explains the lack of strong cooperative SCO and larger hysteresis in this series.

The inertness of the $[Au(CN)_2]^-$ building block against dissociation and increased coordination number makes its structural chemistry much more predictable than that described for $[Ag(CN)_2]^-$. Independently of the length of the bridging organic ligand, all derivatives reported to date can be generically formulated as $\{Fe(L)[Au(CN)_2]_2\}\cdot$Guest [L = bipytz,[10a] 3,6-bis(4-pyridyl)-1,2-diazine (bipydz),[10a,10b] bpp,[12] dpb,[13] pz,[8] and Fpz;[9] Scheme 1]. Like **2**, all of these derivatives share the same structural features, that is, twofold interpenetrating α-Po networks, as already discussed for $\{Fe(pz)[Ag(CN)_2]_2\}$ (Scheme 1). For the shortest members of the series, pz and Fpz, the resulting more densely packed framework without accessible voids show highly cooperative SCO properties with wide hysteresis loops of ca. 20 and 40 K, respectively, at relatively high temperatures. However, the cooperativity decreases markedly for the remaining members of the series as the length of the organic bridging ligand increases. Nevertheless, the presence of suitable guest molecules in the pores modulates and enhances the cooperative response of the bpp, dpb, and bipytz derivatives. Although the 2,6-naphthy ligand is closer in the size to pz and Fpz than to bipydz, dpb, or bpp, the resulting compound **2** displays characteristic 1D channels along [001] with 1/2 of a nitrobenzene molecule per Fe^{II} ion, and the nitrobenzene molecules display short π–π interactions with the host 2,6-naphthy ligands. Furthermore, interpenetration leads to aurophilic interactions between the nets in **2** (the $Au^I\cdots Au^I$ distances are ca. 3.16 Å) that are significantly shorter than those observed for the pz and Fpz counterparts.

Conclusions

Two new dimetallic Fe^{II}–M^I (M^I = Ag and Au) cyanido-bridged 3D frameworks based on the ditopic 2,6-naphthy ligand, namely, $\{Fe(2,6\text{-naphthy})[Ag(CN)_2][Ag_2(CN)_3]_2\}$ (**1**) and $\{Fe(2,6\text{-naphthy})[Au(CN)_2]_2\}\cdot 0.5PhNO_2$ (**2**), were synthesized by slow liquid–liquid diffusion techniques. Compound **1** exhibits the rare in situ generated $[Ag_2(CN)_3]^-$ species, which are incorporated in the $\{Fe[Ag(CN)_2][Ag_2(CN)_3]\}_n$ layers connected by pillars of 2,6-naphthy ligands that "thread" the meshes of adjacent networks and lead to a triple interpenetrated 3D framework. This densely packed structure prevents guest inclusion. Moreover, short $Ag\cdots Ag$ contacts evidence the occurrence of argentophilic interactions between the 3D interpenetrated networks. On the other hand, **2** consists of two interpenetrated 3D networks made up of 2D $\{Fe[Au(CN)_2]_2\}_\infty$ layers connected by pillars of 2,6-naphthy ligands, which are axially coordinated to the Fe^{II} ions. Interestingly, 1D channels within this pillared structure house nitrobenzene guest molecules, which are stabilized by host–guest π–π intermolecular interactions and strong aurophilic interactions between the interpenetrated 3D networks. Compounds **1** and **2** with different structural architectures originate two distinct SCO behaviors. Compound **1** features a more abrupt two-step spin transition in a temperature interval of 23 K, whereas **2** shows a much more gradual spin transition that extends over 150 K. Despite this difference, both compounds exhibit unsymmetrical hysteresis loops ca. 6 K wide.

Experimental Section

Materials: $K[Ag(CN)_2]$, $K[Au(CN)_2]$, and $Fe(BF_4)_2\cdot 6H_2O$ were purchased from commercial sources and used as received, whereas the

Table 3. Crystal data for **1** and **2**.

Compound	**1** (250 K)	**1** (150 K)	**2** (250 K)
Empirical formula	$C_{13}H_6Ag_3FeN_7$		$C_{15}H_{8.5}Au_2FeN_{6.5}O$
M_r	639.69		745.57
Crystal system	monoclinic		triclinic
Space group	Pc		$P\bar{1}$
Temperature [K]	250K	150	250
a [Å]	9.3760(8)	8.991(5)	9.4548(9)
b [Å]	10.6240(8)	10.255(5)	10.4730(9)
c [Å]	11.2753(9)	11.110(4)	10.4975(12)
α [°]	90	90	83.369(9)
β [°]	126.714(9)	126.22(3)	85.076(9)
γ [°]	90	90	80.288(8)
V [Å^3]	900.3(2)	826.4(7)	1015.4(2)
Z	2		2
$D_{calcd.}$ [mg cm^{-3}]	2.360	2.571	2.439
$F(000)$	600		672
μ (Mo-K_α) [mm^{-1}]	4.012	4.371	15.133
Crystal size [mm]	0.06 × 0.06 × 0.10		0.08 × 0.08 × 0.18
Total reflections	3389	3307	5127
Reflections [$I > 2\sigma(I)$]	3076	3064	3187
R [$I > 2\sigma(I)$][a]	0.0684	0.0637	0.1033
R [all data][a]	0.0753	0.0685	0.1402
S	1.176	0.836	1.021

[a] $R1 = \Sigma ||F_o| - |F_c||/\Sigma |F_o|$; $wR = \{\Sigma [w(F_o^2 - F_c^2)^2]/\Sigma [w(F_o^2)^2]\}^{1/2}$; $w = 1/[\sigma^2(F_o^2) + (mP)^2 + nP]$; $P = (F_o^2 + 2F_c^2)/3$; $m = 0.1090$ [**1** (250 K)], 0.1029 [**1** (150 K)], 0.1886 [**2** (250 K)]; $n = 1.5595$ [**1** (250 K)], 29.0173 [**1** (150 K)].

2,6-naphthy ligand was synthesized as described in Section 1.8.1 in the Supporting Information.

Crystal Growth: Single crystals of **1** were grown by a slow liquid–liquid diffusion technique with a modified H-vessel with a third tube. The peripheral tubes (total volume ca. 10 mL) contained $Fe(BF_4)_2 \cdot 6H_2O$ (0.077 mmol, 26 mg) and $K[Ag(CN)_2]$ (0.154 mmol, 30.6 mg). The central tube (total volume ca. 10 mL) contained the 2,6-naphthy ligand (0.077 mmol, 10 mg). Each individual tube was filled with H_2O/MeOH (1:1). Afterwards, the tubes were sealed with parafilm. Four weeks later, red rodlike single crystals formed in relatively high yield (ca. 50 %) in the tube that originally contained $Fe(BF_4)_2 \cdot 6H_2O$. $C_{13}H_6Ag_3FeN_7$ (639.69): calcd. C 24.38, H 0.94, N 15.32; found C 23.90, H 0.92, N 15.10.

Yellow rodlike single crystals of **2** (yield ca. 50 %) were grown in an H-tube (total volume ca. 10 mL). One tube contained $Fe(BF_4)_2 \cdot 6H_2O$ (0.077 mmol, 26 mg) and the 2,6-naphthy ligand (0.077 mmol, 10 mg) and the other contained $K[Au(CN)_2]$ (0.154 mmol, 44.4 mg). Each individual tube was filled with MeOH and then $PhNO_2$/MeOH (1:10). Finally, the tubes were sealed with parafilm. The presence and quantification of the guest molecules were determined through thermogravimetric analysis (TGA) and confirmed by single-crystal X-ray diffraction. $C_{15}H_{8.5}Au_2FeN_{6.5}O$ (745.57): calcd. C 24.14, H 1.14, N 12.20; found C 24.51, H 1.16, N 12.35.

Physical Characterization: Variable-temperature magnetic susceptibility measurements were performed with single crystals (15–20 mg) of the title compounds with a Quantum Design MPMS2 superconducting quantum interference device (SQUID) susceptometer equipped with a 5.5 T magnet and operating at 1 T and at temperatures from 300–1.8 K.

The calorimetric measurements were performed with a Mettler Toledo DSC 821e differential scanning calorimeter. Low temperatures were obtained with an aluminium block attached to the sample holder, refrigerated with a flow of liquid nitrogen, and stabilized at a temperature of 110 K. The sample holder was kept in a dry box under a flow of dry nitrogen gas to avoid water condensation. The measurements were performed with single crystals of **1** (ca. 20 mg) sealed in aluminium pans with a mechanical crimp. Temperature and heat-flow calibrations were performed with standard samples of indium at its melting transition (429.6 K, 28.45 J g^{-1}). Overall accuracies of ±0.2 K in temperature and ±2 % in the heat capacity were estimated. The uncertainty increased for the determination of the anomalous enthalpy and entropy owing to the subtraction of an unknown baseline.

The single-crystal X-ray data were collected with an Oxford Diffraction Supernova diffractometer. In all cases, Mo-K_α radiation (λ = 0.71073 Å) was used. Data scaling and empirical or multiscan absorption corrections were performed. The structures were solved by direct methods with SHELXS-2014 and refined by full-matrix least-squares techniques on F^2 with SHELXL-2014.[19] Non-hydrogen atoms were refined anisotropically, and hydrogen atoms were placed in calculated positions and refined in idealized geometries (riding model) with fixed isotropic displacement parameters. The relevant crystallographic data for **1** and **2** are gathered in Table 3. Compound **1** shows thermal disorder at 250 and 150 K as well as residual electron density (3.68–4.49 e Å^{-3}) located very close to the Ag sites at 150 K (alerts A and B). The nitrobenzene guest molecules in **2** show thermal disorder at 250 K (alerts A and B), and residual electron density (2.48–10.94 e Å^{-3}) is located very close to the Fe and Au atoms (alerts A and B). However, the structures of the host frameworks and generally those of the guest molecules were reasonably well determined. More importantly, they fully convey all of the chemical and structural meaning required to explain correctly the spin-crossover behavior in this series of compounds and compare well with the data previously reported for other members of the Hofmann-type spin-crossover clathrate family.

.

Acknowledgments

This work was supported by the Spanish Ministerio de Economia y Competitividad (MINECO), Fondos Europeos para el Desarrollo Regional (FEDER) (CTQ2013-46275-P and CTQ2016-78341-P), Unidad de Excelencia María de Maeztu (MDM-2015-0538), and the Generalitat Valenciana through PROMETEO/2016/147. L. P. L. and F. J. V. M. thank the Universidad de Valencia and MINECO, respectively for predoctoral (FPI) grants.

Keywords: N ligands · Metal-organic frameworks · Silver · Gold · Iron · Spin crossover

[1] a) E. König, *Struct. Bonding (Berlin)* **1991**, *76*, 51; b) P. Gütlich, A. Hauser, H. Spiering, *Angew. Chem. Int. Ed. Engl.* **1994**, *33*, 2024; *Angew. Chem.* **1994**, *106*, 2109; c) J. A. Real, A. B. Gaspar, V. Niel, M. C. Muñoz, *Coord. Chem. Rev.* **2003**, *236*, 121; d) P. Gütlich, H. A. Goodwin, Eds. Spin Crossover in Transition Metal Compounds I–III. *Top. Curr. Chem.* **2004**, Vols. *233-235*; e) J. A. Real, A. B. Gaspar, M. C. Muñoz, *Dalton Trans.* **2005**, 2062; f) A. Bousseksou, G. Molnár, L. Salmon, W. Nicolazzi, *Chem. Soc. Rev.* **2011**, *40*, 3313; g) M. A. Halcrow (Ed.), *Spin-crossover materials: properties and applications*. John Wiley & Sons. **2013**.

[2] C. Enachescu, M. Nishino, S. Miyashita in *Spin-crossover materials: properties and applications* (Ed.: M. A. Halcrow), Pages 455–471; John Wiley & Sons. **2013**.

[3] a) O. Kahn, *J. Chem. Phys.* **1988**, *88-89*, 1113; b) O. Kahn, J. P. Launay, *Chemtronics* **1988**, *3*, 140; c) O. Kahn, J. Kröber, C. Jay, *Adv. Mater.* **1992**, *4*, 718; d) O. Kahn, C. J. Martinez, *Science* **1998**, *279*, 279.

[4] a) V. Meded, A. Bagrets, K. Fink, R. Chandrasekar, M. Ruben, F. Evers, A. Bernand-Mantel, J. S. Seldenthuis, A. Beukman, H. S. J. van der Zant, *Phys. Rev. B* **2011**, *83*, 245415; b) F. Prins, M. Monrabal-Capilla, E. A. Osorio, E. Coronado, H. S. J. van der Zant, *Adv. Mater.* **2011**, *23*, 1545; c) M. Cavallini, I. Bergenti, S. Milita, J. C. Kengne, D. Gentili, G. Ruani, I. Salitros, V. Meded, M. Ruben, *Langmuir* **2011**, *27*, 4076; d) T. Miyamachi, M. Gruber, V. Davesne, M. Bowen, S. Boukari, L. Joly, F. Scheurer, G. Rogez, T. K. Yamada, P. Ohresser, E. Beaurepaire, W. Wulfhekel, *Nat. Commun.* **2012**, *3*, 938; e) P. N. Martinho, C. Rajnak, M. Ruben, in *Spin-Crossover Materials: Properties and Applications* (Ed.: M. A. Halcrow), Wiley: **2013**, pp. 376–404 and references cited therein; f) H. J. Shepherd, G. Molnár, W. Nicolazzi, L. Salmon, A. Bousseksou, *Eur. J. Inorg. Chem.* **2013**, 653; g) A. Rotaru, J. Dugay, R. P. Tan, I. A. Guralskiy, L. Salmon, P. Demont, J. Carrey, G. Molnár, M. Respaud, A. Bousseksou, *Adv. Mater.* **2013**, *25*, 1745; h) I. A. Gural'skiy, C. M. Quintero, J. Sánchez-Costa, P. Demont, G. Molnár, L. Salmon, H. J. Shepherd, A. Bousseksou, *J. Mater. Chem. C* **2014**, *2*, 2949; i) A. C. Aragonés, D. Aravena, J. I. Cerdá, Z. Acís-Castillo, H. Li, J. A. Real, F. Sanz, J. Hihath, E. Ruiz, I. Díez-Pérez, *Nano Lett.* **2016**, *16*, 218.

[5] a) J. G. Haasnoot, G. Vos, W. L. Groeneveld, *Z. Naturforsch. B* **1977**, *32*, 421; b) L. G. Lavrenova, N. V. Ikorskii, V. A. Varnek, I. M. Oglezneva, S. V. Larionov, *Koord. Khim.* **1986**, *12*, 207; c) L. G. Lavrenova, N. V. Ikorskii, V. A. Varnek, I. M. Oglezneva, S. V. Larionov, *Koord. Khim.* **1990**, *16*, 654; d) W. Vreugdenhil, J. H. van Diemen, R. A. G. De Graaff, J. G. Haasnoot, J. Reedijk, A. M. van der Kraan, O. Kahn, J. Zarembowitch, *Polyhedron* **1990**, *9*, 2971.

[6] a) See ref.[1c]; b) Y. Garcia, V. Niel, M. C. Muñoz, J. A. Real, "Spin crossover in 1D, 2D and 3D polymeric Fe^{II} networks" in *Topics in Current Chemistry Vol. 233: Spin Crossover in Transition Metal Compounds I* (Eds.: P. Gütlich, H. A. Goodwin), Springer, Berlin, **2004**; c) M. C. Muñoz, J. A. Real, "Polymeric Spin-Crossover Materials" in *Spin-Crossover Materials: Properties and Applications* (Ed.: M. A. Halcrow), John Wiley & Sons, Chichester, **2013**; d) M. C. Muñoz, J. A. Real, *Coord. Chem. Rev.* **2011**, *255*, 2068; e) M. L. Tong, *Coord. Chem. Rev.* **2017**, *335*, 28.

[7] V. Niel, M. C. Muñoz, A. B. Gaspar, A. Galet, G. Levchenko, J. A. Real, *Chem. Eur. J.* **2002**, *8*, 2446.

[8] a) I. A. Gural'skiy, S. I. Shylin, B. O. Golub, V. Ksenofontov, I. O. Fritsky, W. Tremel, *New J. Chem.* **2016**, *40*, 9012; b) I. A. Gural'skiy, B. O. Golub, S. I. Shylin, V. Ksenofontov, H. J. Shepherd, P. R. Raithby, W. Tremel, I. O. Fritsky, *Eur. J. Inorg. Chem.* **2016**, 3191.

[9] F. J. Valverde-Muñoz, M. Seredyuk, M. C. Muñoz, K. Znovjyak, I. O. Fritsky, J. A. Real, *Inorg. Chem.* **2016**, *55*, 10654.

[10] a) J. E. Clements, J. R. Price, S. M. Neville, C. J. Kepert, *Angew. Chem. Int. Ed.* **2014**, *53*, 10164; *Angew. Chem.* **2014**, *126*, 10328; b) J. E. Clements, J. R. Price, S. M. Neville, C. J. Kepert, *Angew. Chem. Int. Ed.* **2016**, *55*, 15105; *Angew. Chem.* **2016**, *128*, 15329.

[11] J.-Y. Li, Z.-P. Ni, Z. Yan, Z.-M. Zhang, Y.-C. Chen, W. Liu, M.-L. Tong, *CrystEngComm* **2014**, *16*, 6444.

[12] J.-Y. Li, Y.-C. Chen, Z.-M. Zhang, W. Liu, Z.-P. Ni, M.-L. Tong, *Chem. Eur. J.* **2015**, *21*, 1645.

[13] J.-Y. Li, C.-T. He, Y.-C. Chen, Z.-M. Zhang, W. Liu, Z.-P. Ni, M.-L. Tong, *J. Mater. Chem. C* **2015**, *3*, 7830.

[14] a) V. Niel, A. L. Thompson, A. E. Goeta, C. Enachescu, A. Hauser, A. Galet, M. C. Muñoz, J. A. Real, *Chem. Eur. J.* **2005**, *11*, 2047; b) T. Kosone, Y. Suzuki, S. Ono, C. Kanadani, T. Saito, T. Kitazawa, *Dalton Trans.* **2010**, *39*, 1786; c) J.-Y. Li, Z. Yan, Z.-P. Ni, Z.-M. Zhang, Y.-C. Chen, W. Liu, M.-L. Tong, *Inorg. Chem.* **2014**, *53*, 4039.

[15] M. C. Muñoz, A. B. Gaspar, A. Galet, J. A. Real, *Inorg. Chem.* **2007**, *46*, 8182.

[16] A. Galet, M. C. Muñoz, A. B. Gaspar, J. A. Real, *Inorg. Chem.* **2005**, *44*, 8749.

[17] See ref.[14]

[18] T. Soma, T. Iwamoto, *Angew. Chem. Int. Ed. Engl.* **1994**, *33*, 1665; *Angew. Chem.* **1994**, *106*, 1746.

[19] a) G. M. Sheldrick, *Acta Crystallogr., Sect. A: Found. Crystallogr.* **2008**, *64*, 112; b) G. M. Sheldrick, *SHELXL-2014*, University of Göttingen, **2014**.